CLL–ZCS Resonant Converter

Model Description and Harmonics Compensator Design

Alintel srl - Davide Bagnara

October 5, 2022

Contents

List of Figures

List of Tables

Chapter 1

CLL–ZCS Resonant Converter

Nomenclature

Here the list of variables and parameters used along the document:

- v_{rst}^{grid} $\left[\mathrm{V}\right]$: grid phase voltage;

- v_{dc} $\left[\mathrm{V}\right]$: dc–link voltage;

- i_s $\left[\mathrm{A}\right]$: internal current of the resonant circuit;

- v_s^{in} $\left[\mathrm{V}\right]$: input voltage of the resonant circuit;

- v_s^{out} $\left[\mathrm{V}\right]$: output voltage of the resonant circuit;

- v_{out} $\left[\mathrm{V}\right]$: load voltage;

- i_{out} $\left[\mathrm{A}\right]$: load current;

- C_1, C_2 $\left[\mathrm{F}\right]$: dc–link capacitors;

- L_s $\left[\mathrm{H}\right]$: series inductance of the resonant circuit;

- L_p $\left[\mathrm{H}\right]$: parallel inductance of the resonant circuit;

- C_s $\left[\mathrm{F}\right]$: series capacitance of the resonant circuit;

- L_{ds} $\left[\mathrm{H}\right]$: leakage inductance of the high-frequency single phase transformer;

- L_m $\left[\mathrm{H}\right]$: magnetization inductance of the high-frequency single phase transformer;

- C_{Fu} $\left[\mathrm{F}\right]$: output filter capacitance;

– n_1 $\left[\ \right]$: number of turns at primary side of the high-frequency single phase transformer;

– n_2 $\left[\ \right]$: number of turns at secondary side of the high-frequency single phase transformer;

1.1   Model Description

In this section the electrical topology of the CLL–ZCS resonant converter is presented. Figure 1.1 shows the complete topology, where the following parts are depicted:

– an input stage uncontrolled rectifier (see Figure 1.1b) – *AC/DC*;

– an half bridge switching converter (see Figure 1.1a) – *DC/AC*;

– a double resonance circuit – $C_s L_s L_p$;

– an high frequency transformer with scaling n_1/n_2;

– an output stage uncontrolled rectifier – *AC/DC*;

– an output stage filter C_{Fu} with a bleeder load R_b;
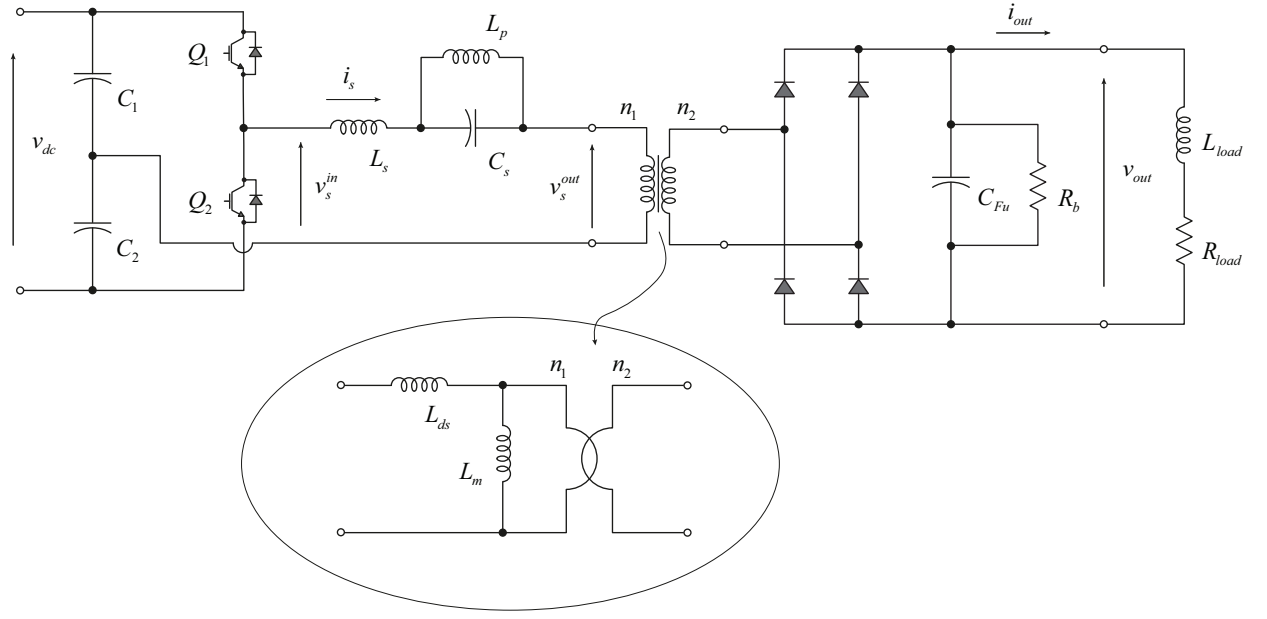
(a) CLL–ZCS resonant converter output stage.
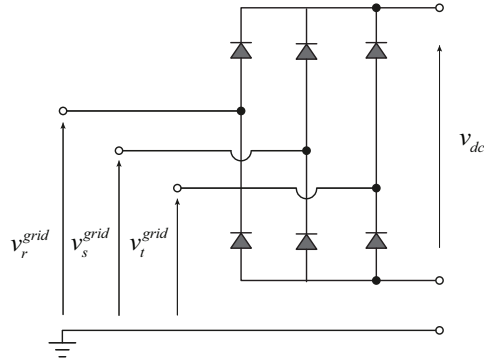
(b) CLL–ZCS resonant converter input stage rectifier.

Figure 1.1: CLL–ZCS resonant converter.

During the normal operation, the half bridge generates a fixed t_{on} pulse with variable modulation index $m = t_{on}/t_{sw}$ that means the switching frequency $f_{sw} = 1/t_{sw}$ will be selected in a range between the minimum resonance frequency $f_{sw}^{min} = f_{rp}$ and around half of the maximum resonance frequency f_{rs} i.e. $f_{sw}^{max} \approx f_{rs}/2$. The resonance block circuit is made by the coupling of two LC circuits:

  – one series L_sC_s, which becomes a short-circuit at f_{rs} resonance frequency;

  – one parallel L_pC_s, which becomes an open-circuit at f_{rp} resonance frequency;

The resonance block is also depicted in Figure 1.2a.

As above mentioned the resonance block can be splitted into two resonance LC circuits,

respectively as follows:

$$z_p(s) = \frac{sL_p}{s^2 L_p C_s + 1} \tag{1.1.1}$$

$$z_s(s) = \frac{s^2 L_s C_s + 1}{sC_s} \tag{1.1.2}$$

which results in the following boundary frequencies:

$$\omega_{rp}^2 L_p C_s - 1 = 0 \quad \Rightarrow \quad f_{rp} = \frac{1}{2\pi\sqrt{L_p C_s}} \tag{1.1.3}$$

$$\omega_{rs}^2 L_s C_s - 1 = 0 \quad \Rightarrow \quad f_{rs} = \frac{1}{2\pi\sqrt{L_s C_s}} \tag{1.1.4}$$

At frequency f_{rp} the transfer function between the resonance-circuit voltage input v_s^{in} and the resonance-circuit voltage output v_s^{out} results in a open circuit, while at the frequency $f_{rs} \gg f_{rp}$ results in a short circuit.

Considering the equivalent circuit of Figure 1.2a, the transfer function between the voltage input v_s^{in}, and the voltage output v_s^{out} becomes as follows

$$H_v(v) = \frac{V_s^{out}(s)}{V_s^{in}(s)} = \frac{s^2 R_{load}^{eq} L_p C_s + R_{load}^{eq}}{s^3 R_{load}^{eq} L_s^{eq} L_p C_s + s^2 R_{load}^{eq} L_p C_s + s(L_s^{eq} + L_p) + R_{load}^{eq}} \tag{1.1.5}$$

where $L_s^{eq} = L_s + L_{ds}$ and $R_{load}^{eq} \approx \left(\frac{n_1}{n_2}\right)^2 R_{load}$, and L_{ds} is the leakage transformer inductance.

Plotting the Bode diagram of Eq. (1.1.5) for different values of R_{load}^{eq} the curves reported in Figure 1.2b are obtained. As per Figure 1.2b the attenuation capacity of the *CLL* circuit is function of the load, if he load increases its impedance the corresponding attenuation curve will be pulled up toward a lower level of attenuation.

1.1.1 Modulation Strategy

Considering Q_1 the gate command of the top switch and Q_2 the gate command of the bottom switch, the modulation strategy is depicted in Figure 1.3. The resonance circuit is excited by a fixed t_{on} calculated as follows

$$t_{on} \approx \left(\sqrt{2} f_{rs}\right)^{-1} \tag{1.1.6}$$

the modulation takes its effect changing the timing where both gate command Q_1 and Q_2 are zero. The excitation pulse t_{on} is selected in order to guarantee the zero current switching.
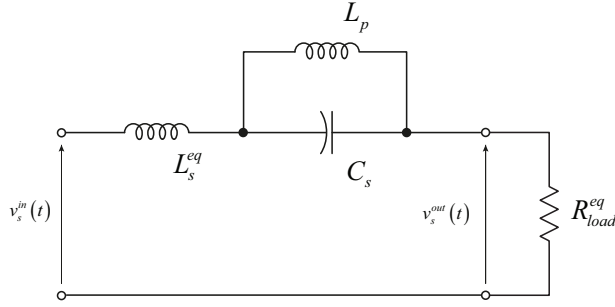
(a) Equivalent circuit of the resonance block.
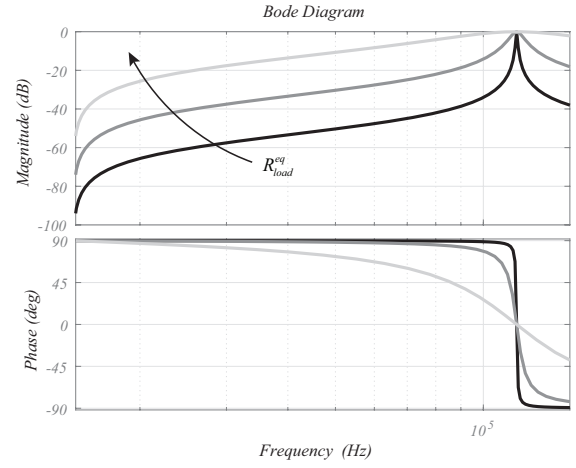
(b) Bode diagram of the equivalent circuit of the resonance block for different values of load.

Figure 1.2: Resonance circuit analysis as function of the load.
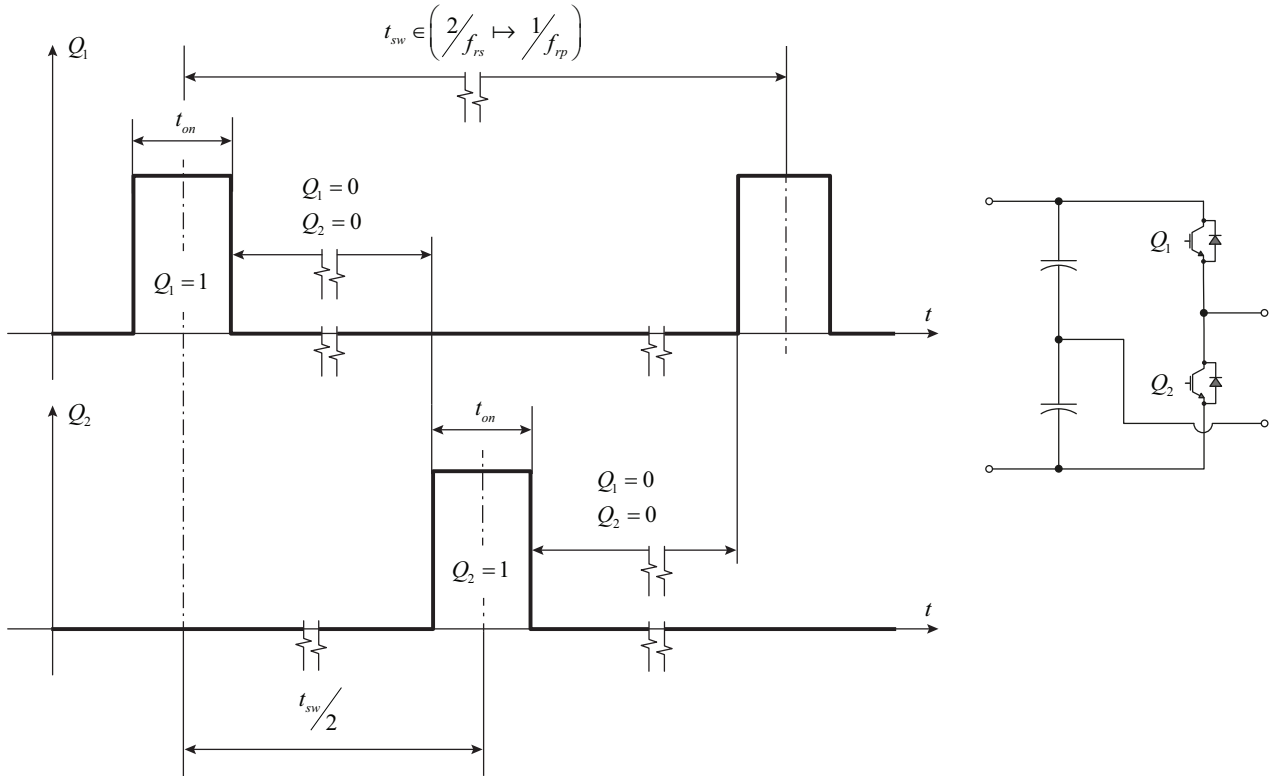
Figure 1.3: Description of the modulation law.

The presence of a not symmetric three phase grid voltage can generate a second harmonic in the dc-voltage of the *DC-link* stage (v_{dc}) as well as a sixth harmonic component due to the diode rectifier. In order to attenuate the effects of these harmonic components into the load, an harmonic compensator will be shown in the next section.

Chapter 2

Harmonics Compensator

2.1 Algorithm Description

The harmonic compensator solution proposed in this section is based on Kalman Filter state observer. For a given harmonic component, e.g. $\omega_{hn} = n\,\omega_{grid}$ where ω_{grid} is the measured grid pulsation by a three-phase *PLL*, the following harmonic state space model is considered:

$$\begin{cases} \dot{x}_1(t) = \omega_{hn}\, x_2(t) \\ \dot{x}_2(t) = -\omega_{hn}\, x_1(t) \end{cases} \tag{2.1.1}$$

which results in the following matrix representation

$$\begin{cases} \dot{\vec{x}}(t) = \tilde{\mathbf{A}}_{hn}\vec{x}(t) \\ h(t) = \mathbf{C}\vec{x}(t) \end{cases} \tag{2.1.2}$$

where $\tilde{\mathbf{A}}_{hn}(t) = \begin{bmatrix} 0 & \omega_{hn}(t) \\ -\omega_{hn}(t) & 0 \end{bmatrix}$ and $\mathbf{C} = \begin{bmatrix} 1 & 0 \end{bmatrix}$. In order to implement the above model in a microcontroller the discretized equivalent model is derived, and after the discretization we obtain the following transition matrix

$$\mathbf{A}_{hn}(k) = \exp\left[\tilde{\mathbf{A}}_{hn}(t)t_s\right] = \begin{bmatrix} \cos[\omega_{hn}(k)t_s] & \sin[\omega_{hn}(k)t_s] \\ -\sin[\omega_{hn}(k)t_s] & \cos[\omega_{hn}(k)t_s] \end{bmatrix} \tag{2.1.3}$$

where t_s is the sampling time.

The Kalman filter state estimator is based on a Luenberger Observer

$$\hat{\vec{x}}(k+1) = \mathbf{A}_{hn}(k)\hat{\vec{x}}(k) + \mathbf{L}\left[y(k) - \mathbf{C}\hat{\vec{x}}(k)\right] \tag{2.1.4}$$

where the observer gain matrix $\mathbf{L}$ is obtained my the minimization of a covariant matrix $\mathbf{P}(k)$ resulting in a time variant observer gain matrix $\mathbf{L}(k)$. The Kalman filter observer algorithm is

here reported:

The Kalman Filter Algorithm become as follows

$$\hat{\bar{x}}(k|k) = \mathbf{A}_{hn}(k)\hat{\bar{x}}(k|k-1) \tag{2.1.5}$$

$$\mathbf{P}(k|k) = \mathbf{A}_{hn}(k)\,\mathbf{P}(k|k-1)\,\mathbf{A}_{hn}^T(k) + \mathbf{Q} \tag{2.1.6}$$

$$\mathbf{L}(k) = \mathbf{P}(k|k)\mathbf{C}^T\left[\mathbf{C}\,\mathbf{P}(k|k)\,\mathbf{C}^T + \mathbf{R}\right]^{-1} \tag{2.1.7}$$

$$\hat{\bar{x}}(k+1|k) = \hat{\bar{x}}(k|k) + \mathbf{L}(k)\left[y(k) - \mathbf{C}\hat{\bar{x}}(k|k)\right] \tag{2.1.8}$$

$$\mathbf{P}(k+1|k) = \left[\mathbf{I} - \mathbf{L}(k)\,\mathbf{C}\right]\mathbf{P}(k|k) \tag{2.1.9}$$

where $y(k) = i_{out}(k)$ is the load current measure.

The state estimation of the Kalman filter state observer are as follows

$$\hat{x}_1(k) = \hat{I}_{hn}(k)\sin[\hat{\vartheta}_{hn}(k)] \tag{2.1.10}$$

$$\hat{x}_2(k) = \hat{I}_{hn}(k)\cos[\hat{\vartheta}_{hn}(k)] \tag{2.1.11}$$

Once the $\hat{x}_1(k)$, $\hat{x}_2(k)$ signals has been extracted from the measured load current $i_{out}(k)$ the corresponding voltage compensation $v_{hn}(k) = k_{hn}\,\hat{x}_2(k)$ is feed forwarded.
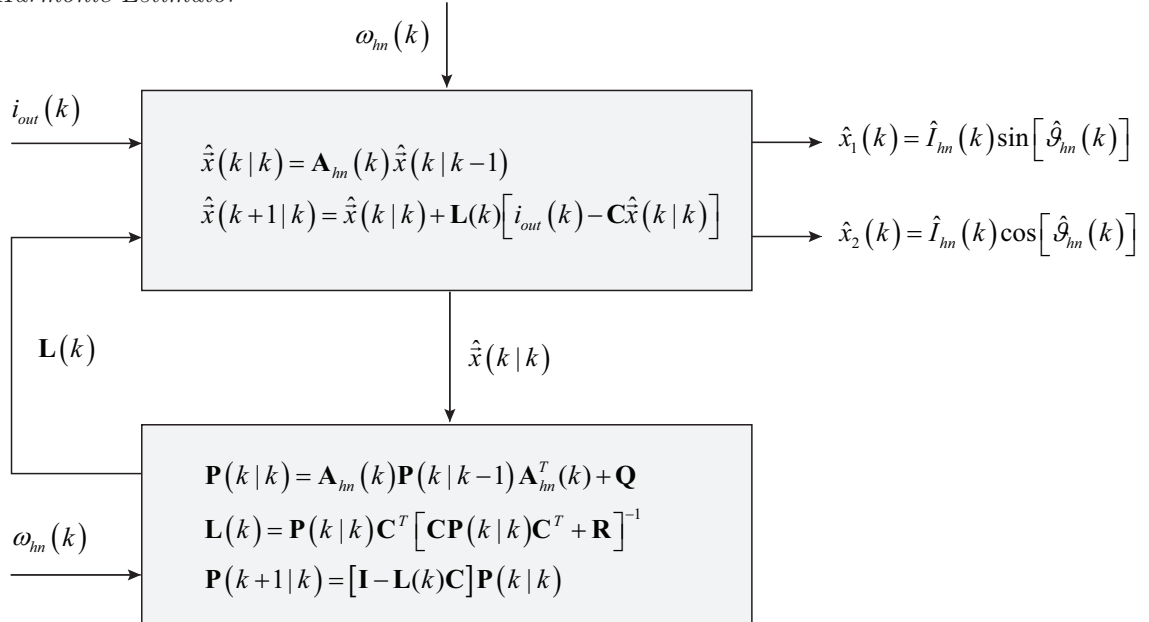
Figure 2.1: Description of the harmonic estimator based on Kalman filter state observer.

To reduce the computing effort of the Kalman filter state observer is possible to implement a steady state version where the matrix gain $\mathbf{L}(k) \rightarrow \mathbf{L}_{kf}$ is off-line pre-calculated resulting in the following structure

$$\hat{\bar{x}}\left(k+1\right) = \mathbf{A}_{hn}(k)\hat{\bar{x}}\left(k\right) + \mathbf{L}_{kf}\left[y(k) - \mathbf{C}\hat{\bar{x}}\left(k\right)\right] \tag{2.1.12}$$

or graphically as shown in Figure 2.2.
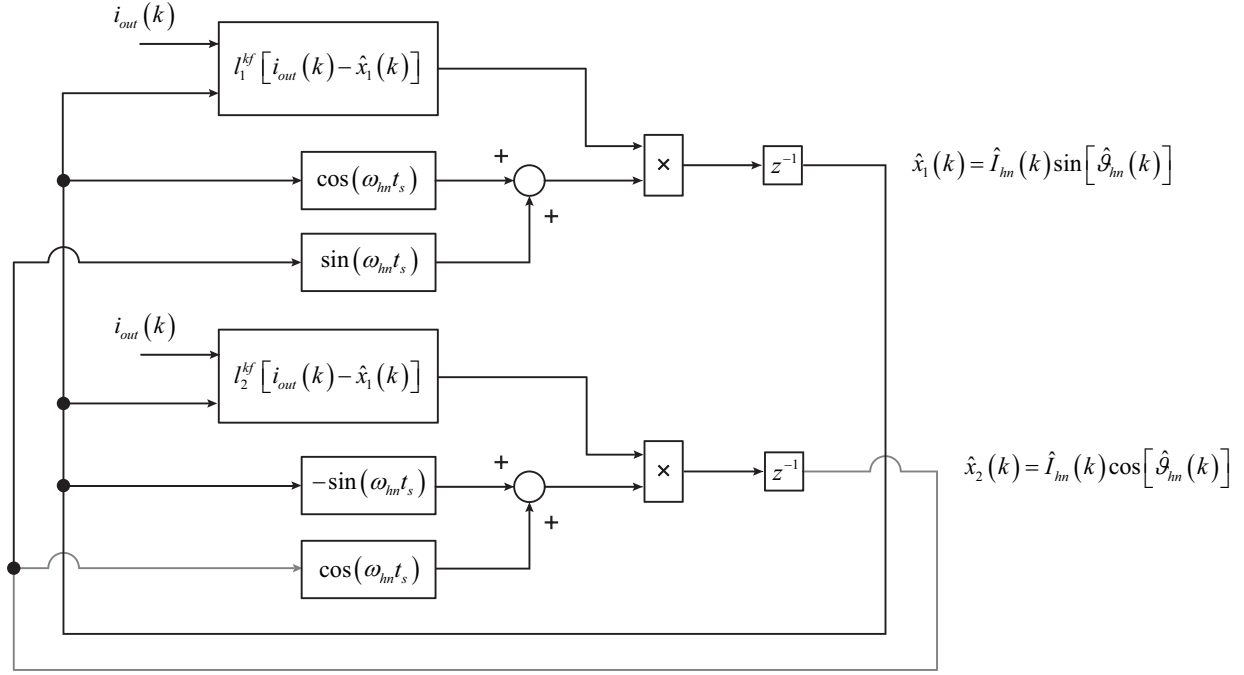
Figure 2.2: Harmonic estimator based on steady state Kalman filter state observer.

2.2 Implementation

The global control of the harmonic compensator merged with the load current control of the *CLL-ZCS* converter is depicted in Figure 2.3. As can be seen from Figure 2.3 the harmonic estimators instances are used to estimate the harmonic signals which affect the load current; from estimation results an open loop compensation is actuated by a simple proportional control gain parameter.
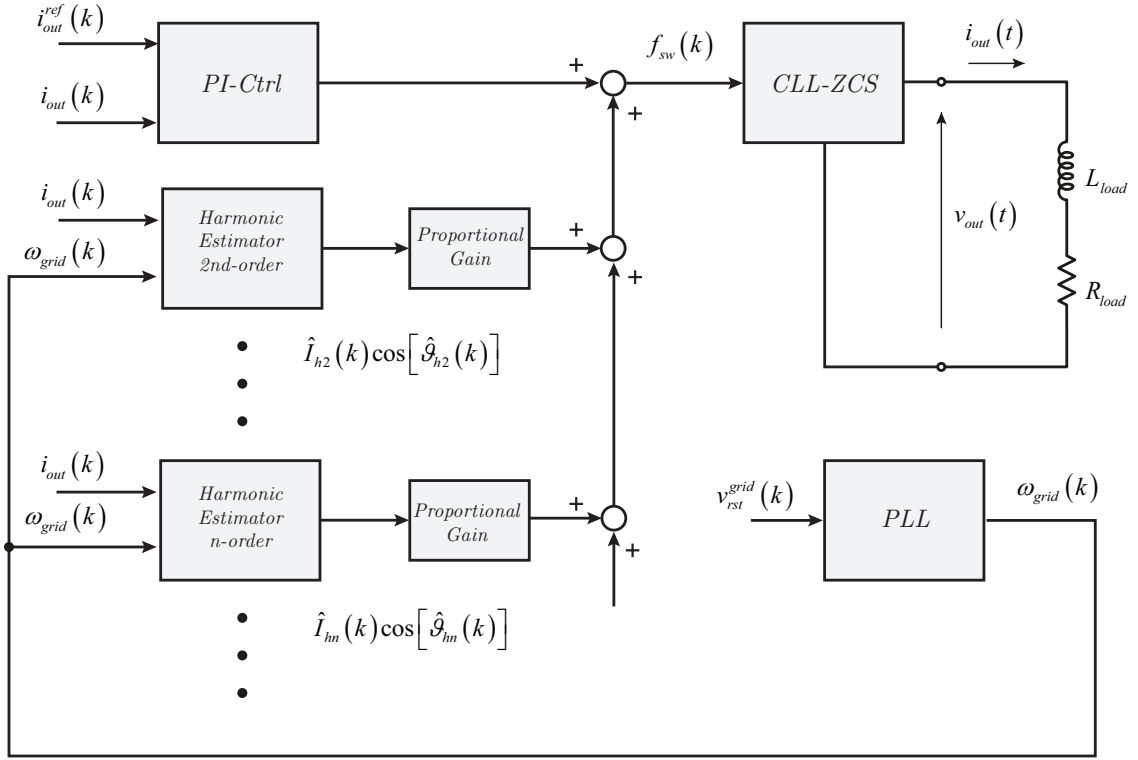
Figure 2.3: Global control architecture for *CLL-ZCS* converter with harmonic load compensator.

Chapter 3

Simulation Results

3.1 CLL–ZCS Simulation Data

For the all simulation reported in this document, the hardware components reported in Table 3.1 are considered.

Component	Value
C_1	$15\,\mu F$
C_1	$15\,\mu F$
L_s	$9.4\,\mu H$
L_p	$1.35\,mH$
C_s	$88\,nF$
L_{ds}	$12\,\mu H$
L_m	$20\,mH$
n_1/n_2	16
C_{F_u}	$264\,\mu F$
R_b	$1.5\,\Omega$

Table 3.1: *CLL-ZCS* hardware components.

3.2 Case study 1

For the first case study the following settings are considered:

- Harmonic compensator is disabled;

- $i_{out}^{ref} = 100\,A$;

– $R_{load} = 0.1\,\Omega$;

– $L_{load} = 25\,\mu\text{H}$.

Figure 3.1: Grid voltage used for the simulation.

(a) Output current and voltage.

(b) Spectrum of the output current.

Figure 3.2: Simulation results - case study 1.

(a) Switch firing command and $i_s(t)$ resonance current.

(b) Control output (frequency switching).

Figure 3.3: Simulation results - case study 1.

3.3   Case study 2

For this second case study the following settings are considered:

– Harmonic compensator enabled;

– $i_{out}^{ref} = 100\,\mathrm{A}$;

– $R_{load} = 0.1\,\Omega$;

– $L_{load} = 25\,\mu\mathrm{H}$.

Figure 3.4: Grid voltage used for the simulation.

(a) Output current and voltage.

(b) Spectrum of the output current.

Figure 3.5: Simulation results - case study 2.

(a) Switch firing command and $i_s(t)$ resonance current.

(b) Control output (frequency switching).

Figure 3.6: Simulation results - case study 2.

3.4 Case study 3

For the third case study the following settings are considered:

- Harmonic compensator is disabled;

- $i_{out}^{ref} = 100\,\text{A}$;

- $R_{load} = 0.1\,\Omega$;
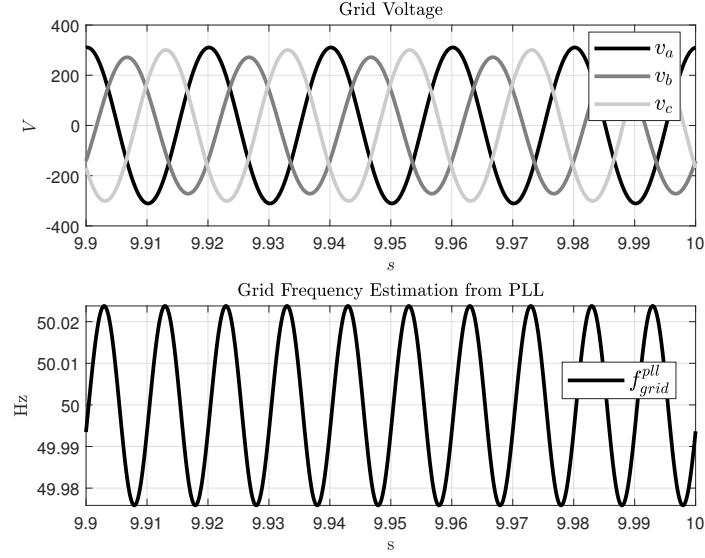
- $L_{load} = 250\,\mu\text{H}$.

Figure 3.7: Grid voltage used for the simulation.

(a) Output current and voltage.

(b) Spectrum of the output current.

Figure 3.8: Simulation results - case study 3.

(a) Switch firing command and $i_s(t)$ resonance current.

(b) Control output (frequency switching).

Figure 3.9: Simulation results - case study 3.

3.5 Case study 4

For this fourth case study the following settings are considered:

- Harmonic compensator enabled;

- $i_{out}^{ref} = 100\,\text{A}$;

- $R_{load} = 0.1\,\Omega$;

- $L_{load} = 250\,\mu\text{H}$.

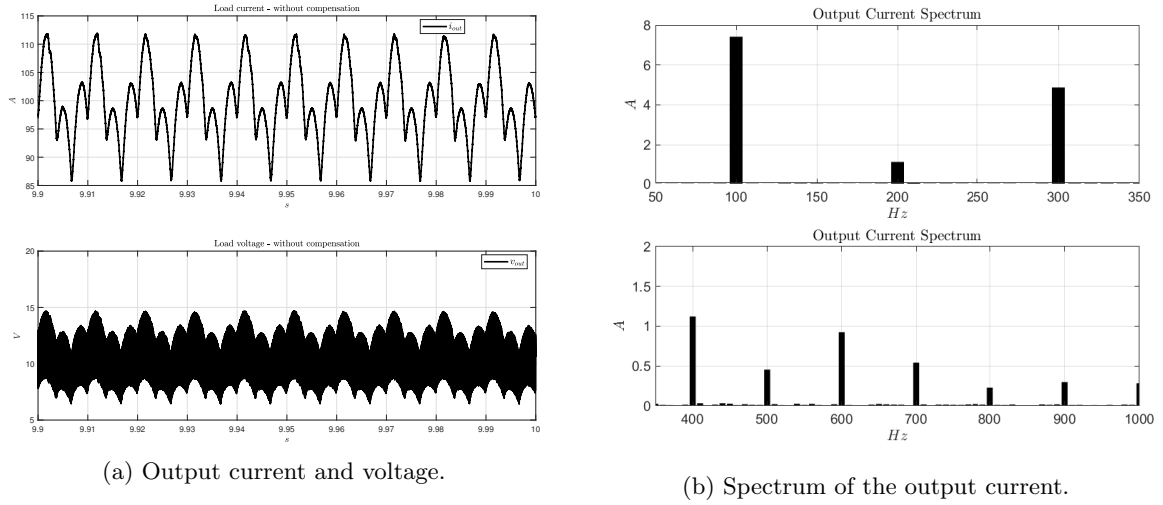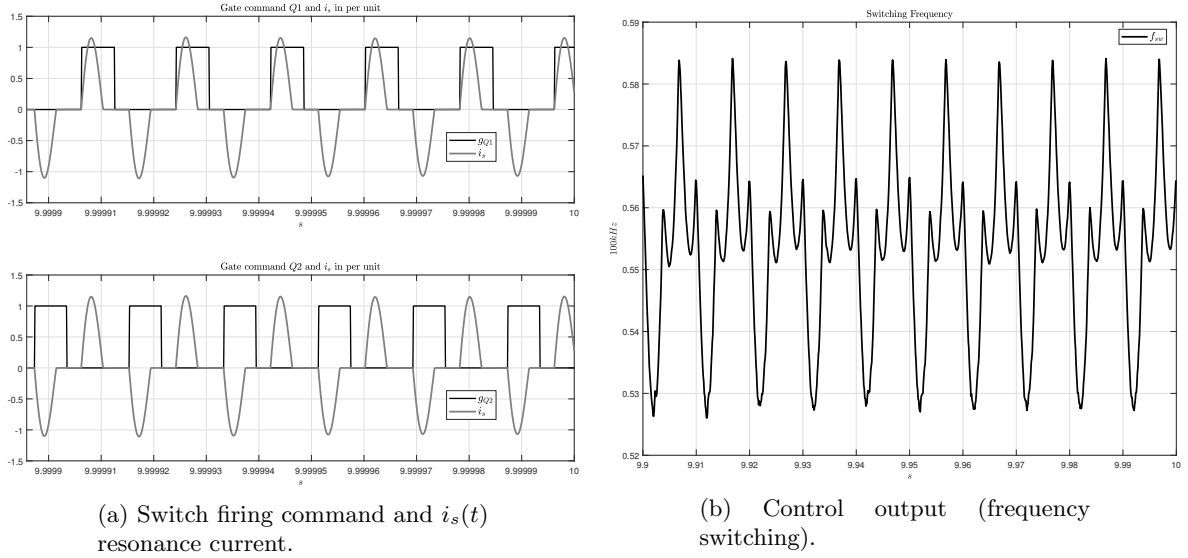Figure 3.10: Grid voltage used for the simulation.

(a) Output current and voltage.

(b) Spectrum of the output current.

Figure 3.11: Simulation results - case study 4.

(a) Switch firing command and $i_s(t)$ resonance current.

(b) Control output (frequency switching).

Figure 3.12: Simulation results - case study 4.

3.6   Case study 5

For the fifth case study the following settings are considered:

- Harmonic compensator is disabled;

- $i_{out}^{ref} = 5\,\text{A}$;

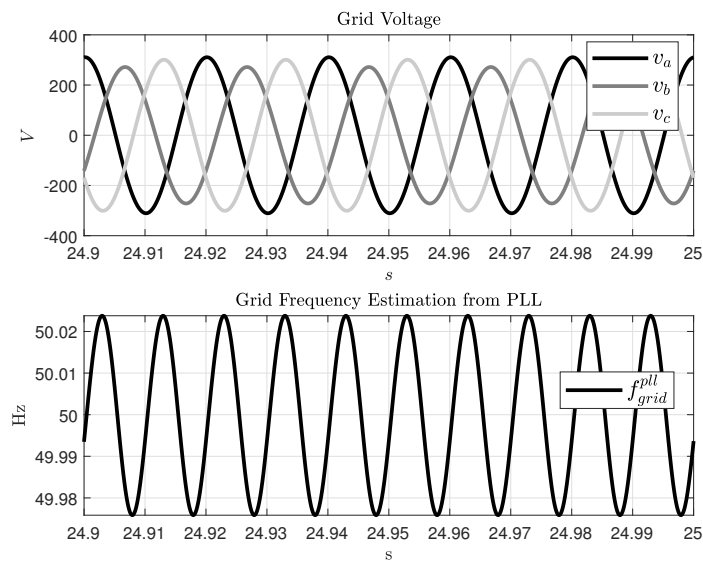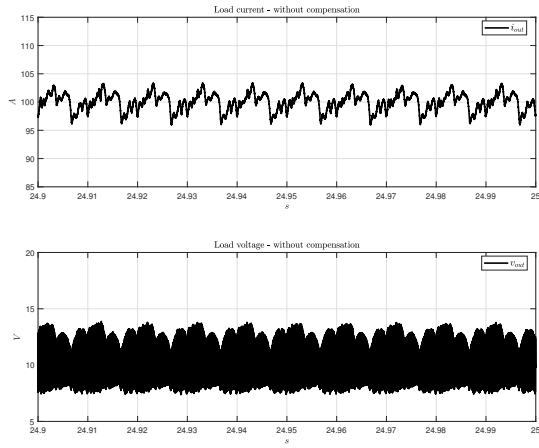- $R_{load} = 2\,\Omega$;
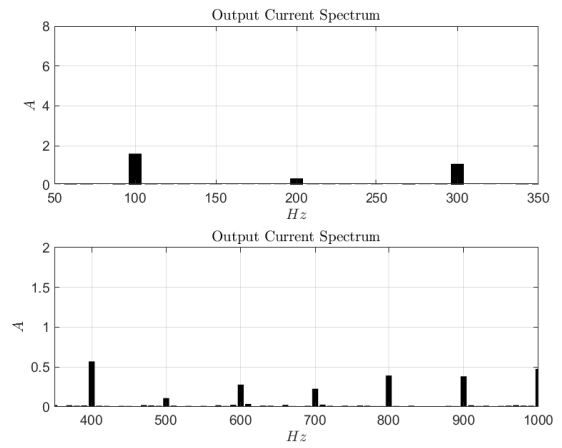
- $L_{load} = 25\,\mu\text{H}$.
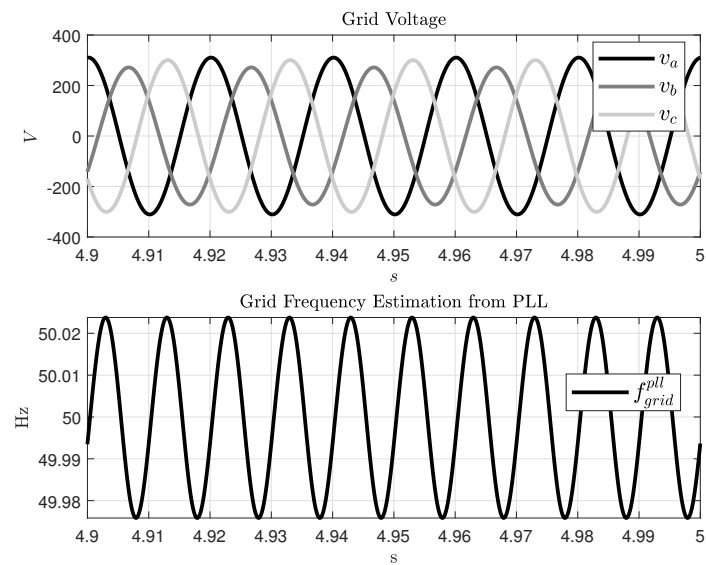
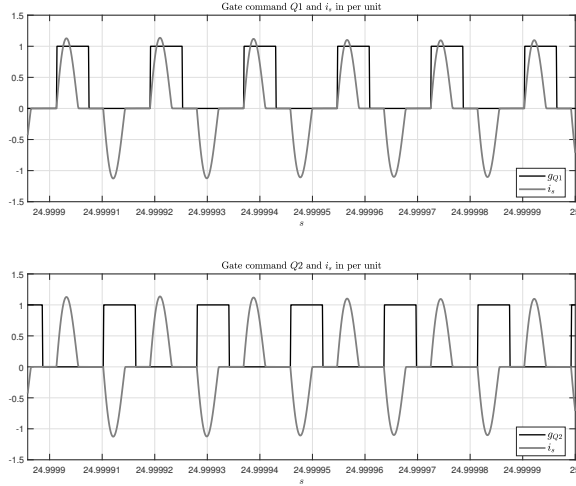Figure 3.13: Grid voltage used for the simulation.
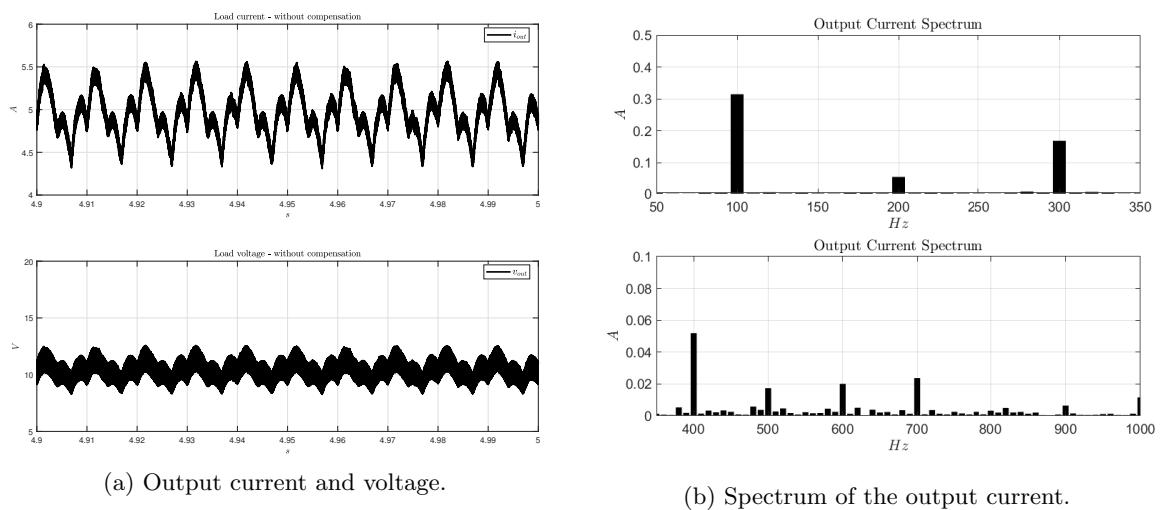
(a) Output current and voltage.

(b) Spectrum of the output current.

Figure 3.14: Simulation results - case study 5.

(a) Switch firing command and $i_s(t)$ resonance current.

(b)   Control   output   (frequency switching).
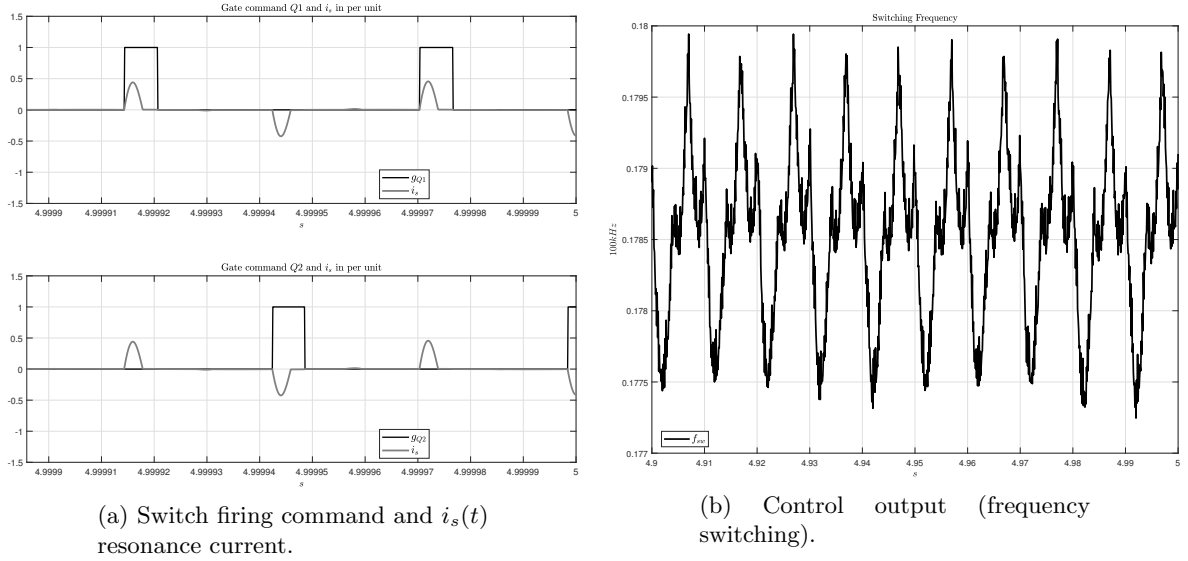
Figure 3.15: Simulation results - case study 5.

3.7   Case study 6

For this sixth case study the following settings are considered:

- Harmonic compensator enabled;

- $i_{out}^{ref} = 5\,\text{A}$;

- $R_{load} = 2\,\Omega$;

- $L_{load} = 25\,\text{µH}$.
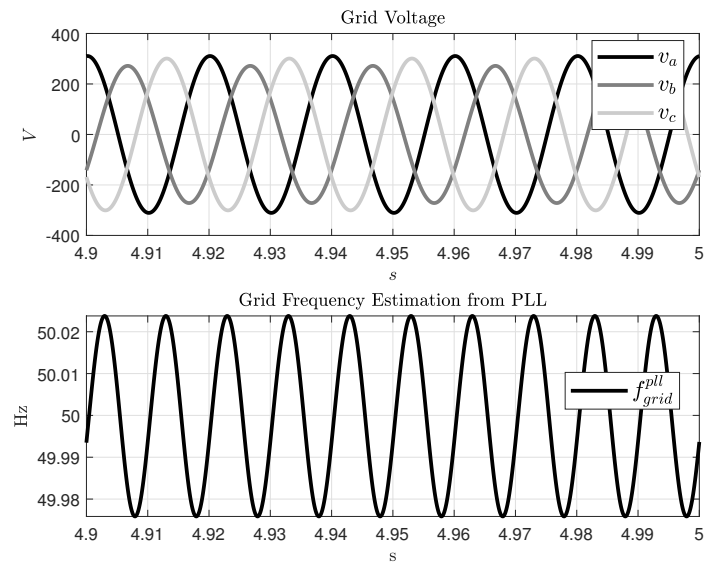
Figure 3.16: Grid voltage used for the simulation.
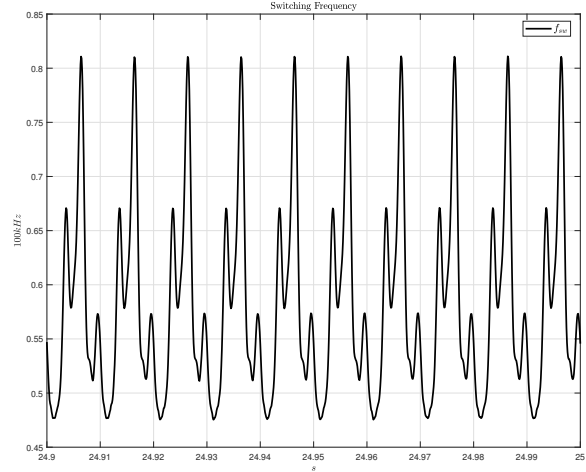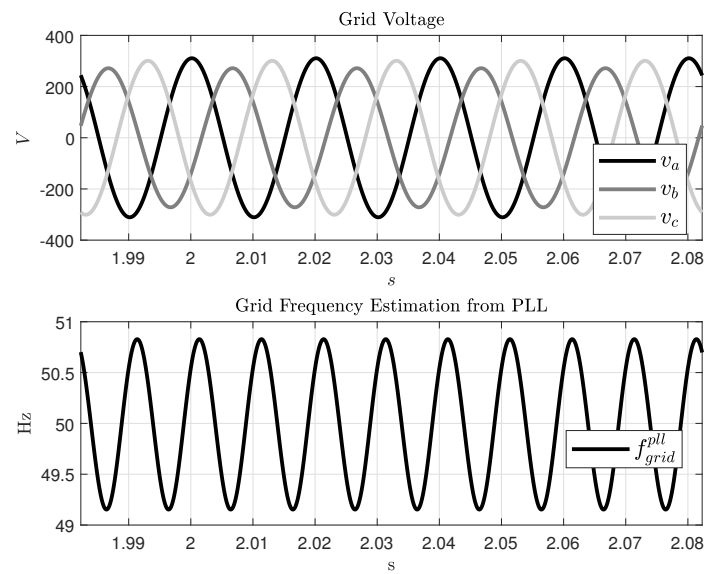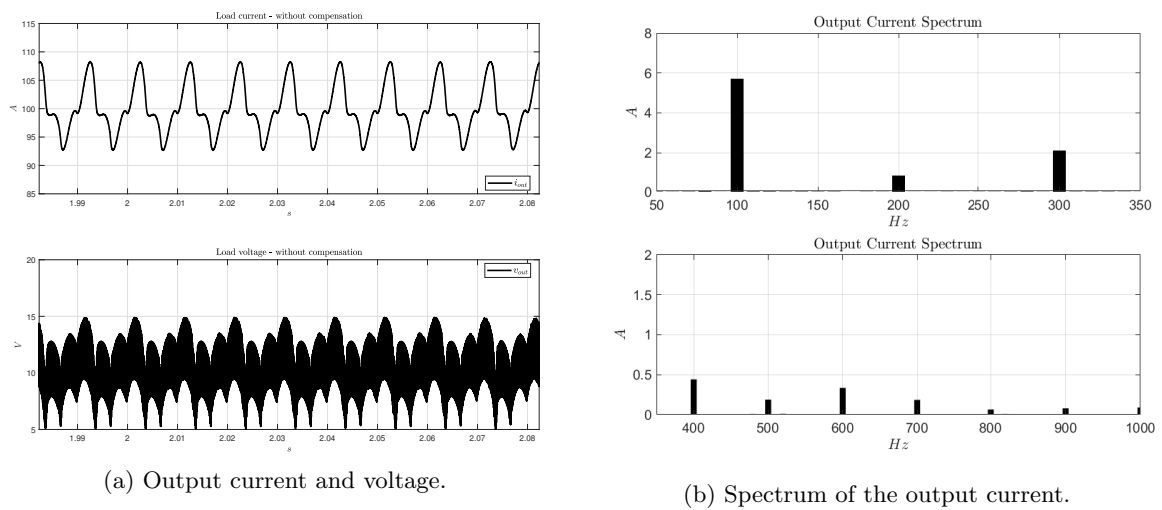
(a) Output current and voltage.

(b) Spectrum of the output current.

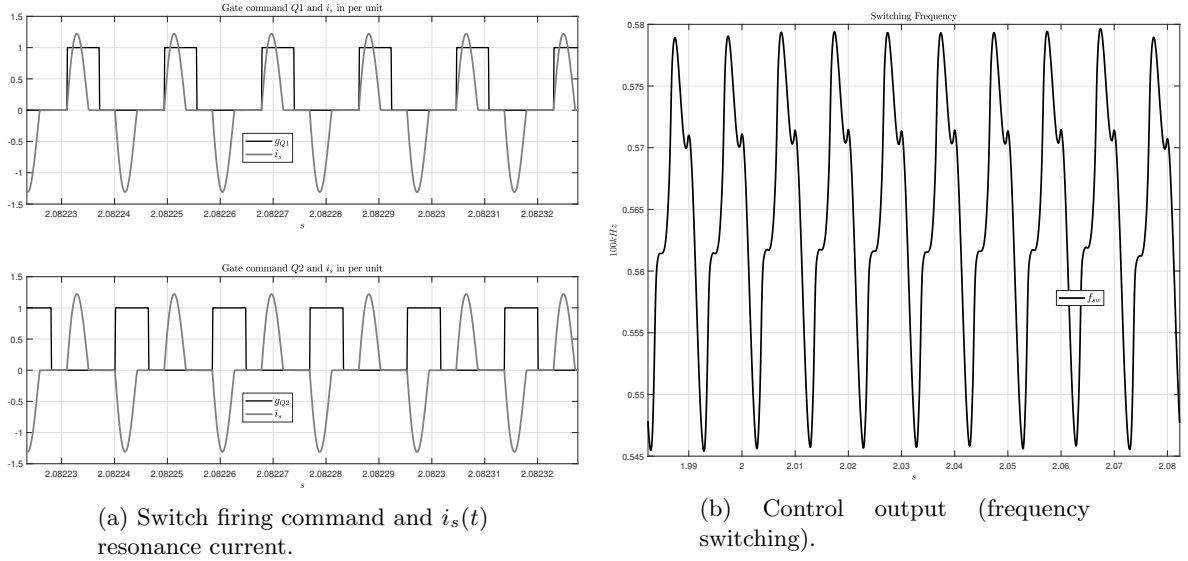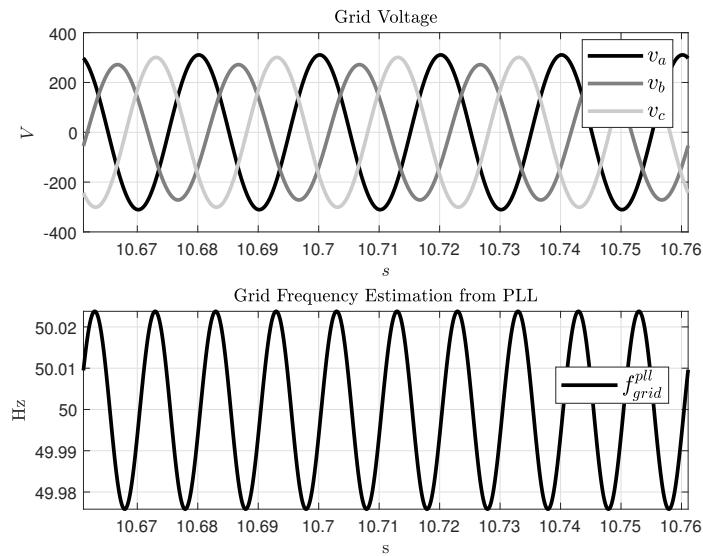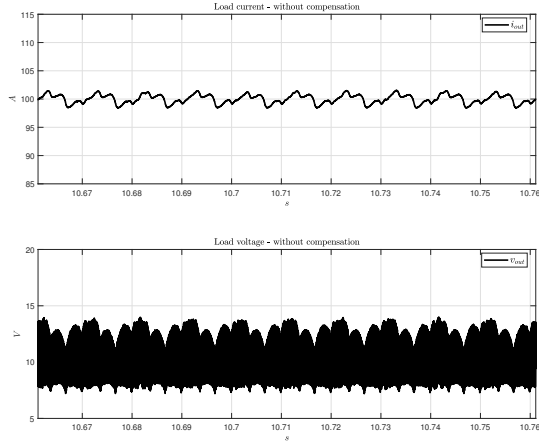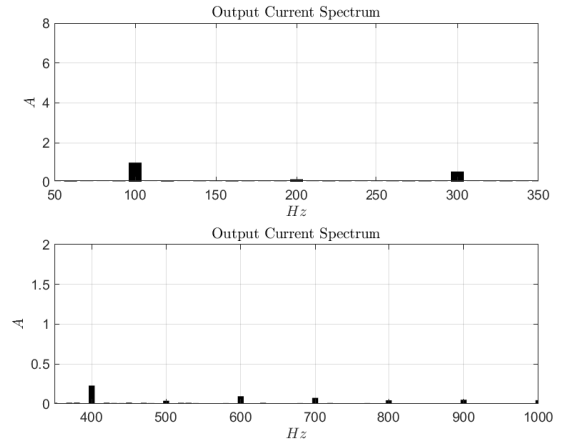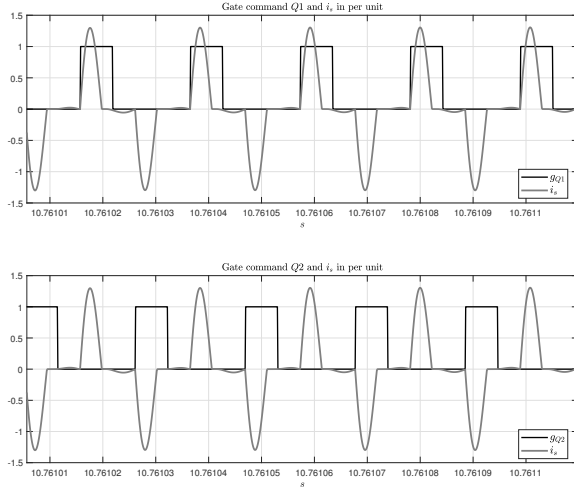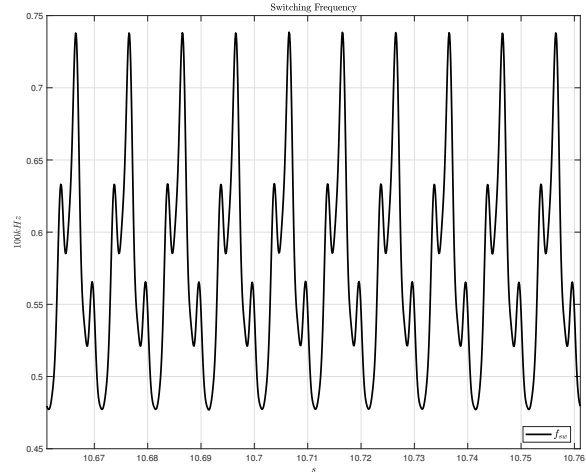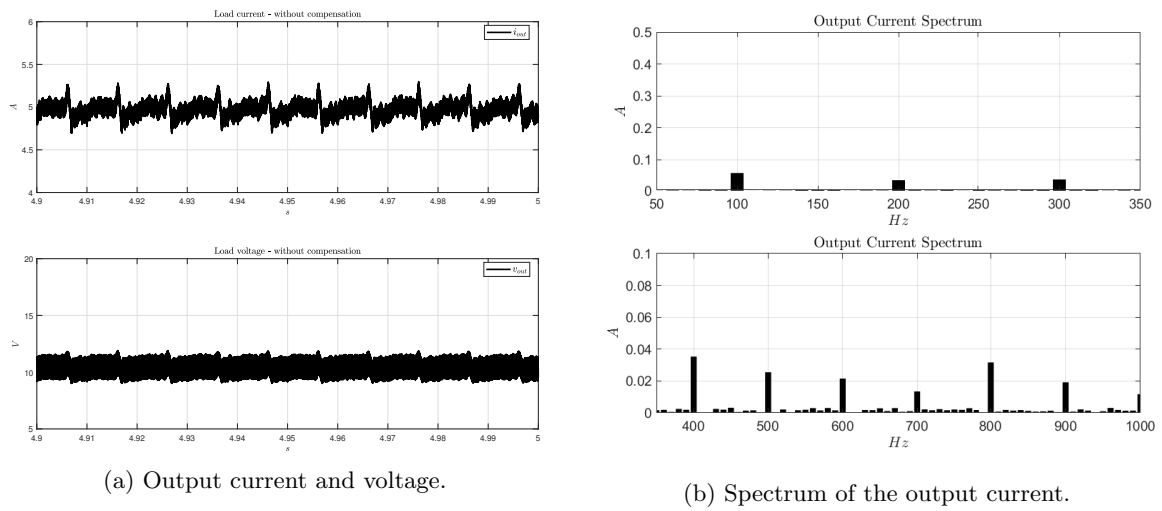Figure 3.17: Simulation results - case study 6.

(a) Switch firing command and $i_s(t)$ resonance current.

(b) Control output (frequency switching).
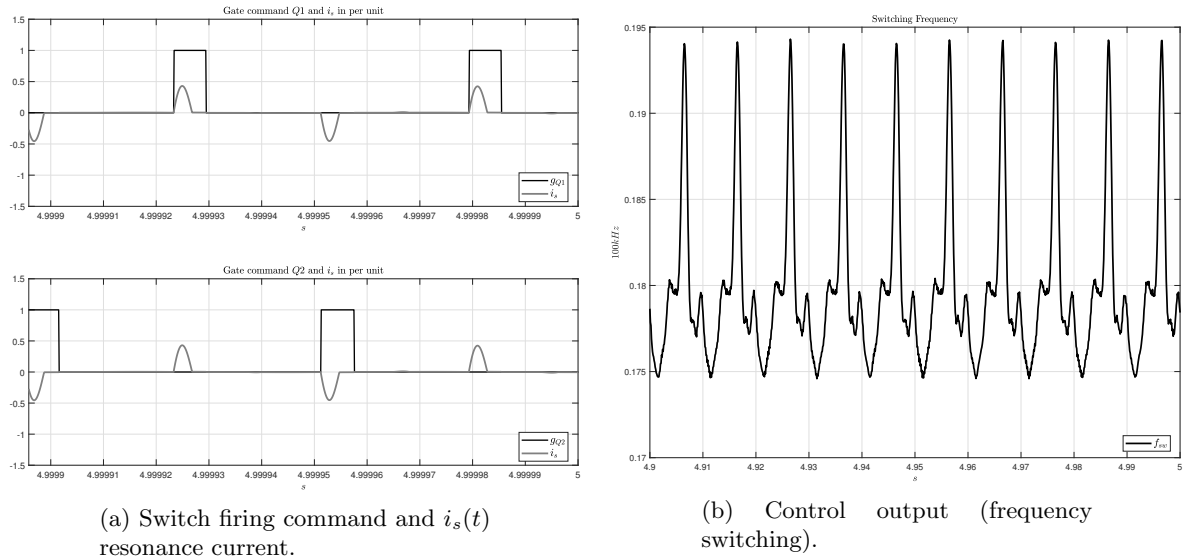
Figure 3.18: Simulation results - case study 6.

Chapter 4

Phase Locked-Loop (PLL) Architecture

4.1   Three-Phase Systems under Unbalanced Conditions

Three-phases voltages can become unbalanced and distorted because of the effect of nonlinear loads and transient grid faults. Ideally, power converters used in distributed generation should be properly synchronized with the grid under such adverse operating conditions to stay actively connected, supporting the grid services and keeping up generation. The faulty three-phase voltages can be generally understood as a summation of unbalanced harmonic components. Therefore, in general way, the three-phase voltage vector can be written as

$$\boldsymbol{v}_{rst} = \begin{bmatrix} v_r \\ v_s \\ v_t \end{bmatrix} = \sum_{n=1}^{\infty} \left(\boldsymbol{v}_{rst}^{+n} + \boldsymbol{v}_{rst}^{-n} + \boldsymbol{v}_{rst}^{0n} \right) \tag{4.1.1}$$

where

$$\boldsymbol{v}_{rst}^{+n} = V^{+n} \begin{bmatrix} \cos\left(n\omega t + \phi^{+n}\right) \\ \cos\left(n\omega t - \frac{2\pi}{3} + \phi^{+n}\right) \\ \cos\left(n\omega t + \frac{2\pi}{3} + \phi^{+n}\right) \end{bmatrix} \tag{4.1.2}$$

$$\boldsymbol{v}_{rst}^{-n} = V^{-n} \begin{bmatrix} \cos\left(n\omega t + \phi^{-n}\right) \\ \cos\left(n\omega t + \frac{2\pi}{3} + \phi^{-n}\right) \\ \cos\left(n\omega t - \frac{2\pi}{3} + \phi^{-n}\right) \end{bmatrix} \tag{4.1.3}$$

$$\boldsymbol{v}_{rst}^{0n} = V^{0n} \begin{bmatrix} \cos\left(n\omega t + \phi^{0n}\right) \\ \cos\left(n\omega t + \phi^{0n}\right) \\ \cos\left(n\omega t + \phi^{0n}\right) \end{bmatrix} \tag{4.1.4}$$

In equations (4.1.1) – (4.1.4), superscripts $+n$, $-n$, and $0n$ respectively represent the positive-, negative-, and zero-sequence components of the nth harmonic of the voltage vector $\boldsymbol{v}$.

Distributed generators are usually linked to three-phase networks by using a three-wire connection and hence they do not inject zero-sequence current into the grid.

The main task, for the grid synchronization here investigated, is to find a method to detect and extract the positive sequence component at the fundamental frequency of the three-phase grid voltages.

In a general form, a positive-sequence voltage vector at the fundamental frequency interacting with either a positive- or negative-sequence nth order component can be expressed as follows

$$\boldsymbol{v}_{rst} = \boldsymbol{v}_{rst}^{+1} + \boldsymbol{v}_{rst}^{n} = V^{+1} \begin{bmatrix} \cos\left(\omega t\right) \\ \cos\left(\omega t - \frac{2\pi}{3}\right) \\ \cos\left(\omega t + \frac{2\pi}{3}\right) \end{bmatrix} + V^{n} \begin{bmatrix} \cos\left(n\omega t\right) \\ \cos\left(n\omega t - \frac{2\pi}{3}\right) \\ \cos\left(n\omega t + \frac{2\pi}{3}\right) \end{bmatrix} \qquad (4.1.5)$$

where $n > 0$ means a positive sequence component and $n < 0$ a negative sequence one.

The voltage vector (4.1.5) can be expressed on the Cartesian $\alpha\beta$ stationary reference frame by using a reduced version of the *Clarke* transformation, resulting in

$$\boldsymbol{v}_{\alpha\beta} = \begin{bmatrix} v_\alpha \\ v_\beta \end{bmatrix} = {}^{rst}\mathbf{T}_{\alpha\beta}\boldsymbol{v}_{rst} = V^{+1} \begin{bmatrix} \cos\left(\omega t\right) \\ \sin\left(\omega t\right) \end{bmatrix} + V^{n} \begin{bmatrix} \cos\left(n\omega t\right) \\ \sin\left(n\omega t\right) \end{bmatrix} \qquad (4.1.6)$$

where

$$ {}^{rst}\mathbf{T}_{\alpha\beta} = \frac{2}{3} \begin{bmatrix} 1 & -\frac{1}{2} & -\frac{1}{2} \\ 0 & \frac{\sqrt{3}}{2} & -\frac{\sqrt{3}}{2} \end{bmatrix} \qquad (4.1.7)$$

The voltage vector (4.1.5) can also be expressed on a Cartesian dq rotating reference frame by using the *Park* transformation as

$$\boldsymbol{v}_{dq} = \begin{bmatrix} v_d \\ v_q \end{bmatrix} = {}^{\alpha\beta}\mathbf{T}_{dq}\boldsymbol{v}_{\alpha\beta} = V^{+1} \begin{bmatrix} \cos\left(\omega t - \vartheta_0\right) \\ \sin\left(\omega t - \vartheta_0\right) \end{bmatrix} + V^{n} \begin{bmatrix} \cos\left(n\omega t - \vartheta_0\right) \\ \sin\left(n\omega t - \vartheta_0\right) \end{bmatrix} \qquad (4.1.8)$$

where

$$ {}^{\alpha\beta}\mathbf{T}_{dq} = \begin{bmatrix} \cos\vartheta_0 & \sin\vartheta_0 \\ -\sin\vartheta_0 & \cos\vartheta_0 \end{bmatrix} \qquad (4.1.9)$$

where ϑ_0 is the angular position of the dq rotating reference frame.

Assuming that the dq reference frame rotates synchronously with the positive-sequence voltage vector, with d-axis in the same direction as the positive-sequence voltage vector $\boldsymbol{v}^{+1}$,

i.e. with $\vartheta_0 = \omega t$, the expression of (4.1.8) results as follows

$$\boldsymbol{v}_{dq} = V^{+1} \begin{bmatrix} 1 \\ 0 \end{bmatrix} + V^n \begin{bmatrix} \cos\left[(n-1)\omega t\right] \\ \sin\left[(n-1)\omega t\right] \end{bmatrix} \tag{4.1.10}$$

From Eq. (4.1.10), the module and the angular position of the three-phase voltage vector, $|\boldsymbol{v}|$ and ϑ respectively are given by

$$|\boldsymbol{v}| = \sqrt{v_\alpha^2 + v_\beta^2} = \sqrt{\left(V^{+1}\right)^2 + \left(V^n\right)^2 + 2V^{+1}V^n \cos\left[(n-1)\omega t\right]} \tag{4.1.11}$$

$$\vartheta = \tan^{-1}\frac{v_\beta}{v_\alpha} = \omega t + \tan^{-1}\left[\frac{V^n \sin\left[(n-1)\omega t\right]}{V^+ + V^n \cos\left[(n-1)\omega t\right]}\right] \tag{4.1.12}$$

Equations (4.1.11) and (4.1.12) shows that the voltage vector $\boldsymbol{v}$ has neither constant module nor rotational frequency. Moreover, these equations show that both the amplitude and the angular position of the positive-sequence component cannot be extracted by just filtering the detected module and phase angle of the compound voltage vector $\boldsymbol{v}$.

4.2 Synchronous Reference Frame PLL (SRF-PLL)

the most extended technique used for frequency-insensitive grid synchronization in the three-phase systems is the PLL based on the synchronous reference frame. The conventional SRF-PLL translates the three-phase voltage vector from the *uvw* fixed reference frame to the rotating *dq* reference frame by using *Park*'s transformation $\mathbf{T}_\vartheta$, as shown in Figure 4.1. The angular position of this *dq* reference frame is controlled by a feedback loop that regulates the *q* component to zero. Eqs. (4.2.1) – (4.2.3) show the main structure of the transformation from fixed reference frame to the synchronous (ϑ) rotating reference frame.
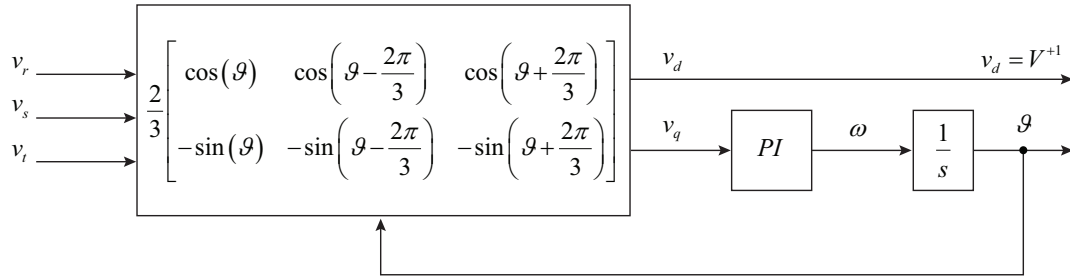
Figure 4.1: SRF PLL architecture.

$$\begin{bmatrix} v_d \\ v_q \end{bmatrix} = \mathbf{T}_\vartheta \begin{bmatrix} v_r \\ v_s \\ v_t \end{bmatrix} \tag{4.2.1}$$

where

$$\mathbf{T}_\vartheta = \frac{2}{3} \begin{bmatrix} \cos(\vartheta) & \cos(\vartheta - \frac{2\pi}{3}) & \cos(\vartheta + \frac{2\pi}{3}) \\ -\sin(\vartheta) & -\sin(\vartheta - \frac{2\pi}{3}) & -\sin(\vartheta + \frac{2\pi}{3}) \end{bmatrix} \tag{4.2.2}$$

$$\mathbf{T}_\vartheta = {}^{\alpha\beta}\mathbf{T}_{dq} {}^{rst}\mathbf{T}_{\alpha\beta} \tag{4.2.3}$$

where

$$^{rst}\mathbf{T}_{\alpha\beta} = \frac{2}{3} \begin{bmatrix} 1 & -\frac{1}{2} & -\frac{1}{2} \\ 0 & \frac{\sqrt{3}}{2} & -\frac{\sqrt{3}}{2} \end{bmatrix} \tag{4.2.4}$$

and

$$^{\alpha\beta}\mathbf{T}_{dq} = \begin{bmatrix} \cos\vartheta & \sin\vartheta \\ -\sin\vartheta & \cos\vartheta \end{bmatrix} \tag{4.2.5}$$

4.3 Decoupled Double Synchronous Reference Frame PLL (DDSRF-PLL)

This section presents an improved three-phase synchronous PLL based on using two synchronous reference frames, rotating with positive and negative synchronous speed, respectively. The usage of this double synchronous reference frame allows decoupling of the effect ot the negative-sequence voltage component on the dq signals detected by the synchronous reference frame rotating with positive angular speed, and vice versa, which makes possible accurate grid synchronization even under unbalanced grid faults.

4.3.1 Double synchronous reference frame

Figure 4.2 shows the positive- and negative-sequence components of the unbalanced voltage vector together with a double synchronous reference frame (DSRF) consisting of two rotating reference frame: dq^{+1}, rotating with the positive speed ω and whose angular position is ϑ, and dq^{-1}, rotating with the negative speed $-\omega$ and whose angular position is $-\vartheta$.
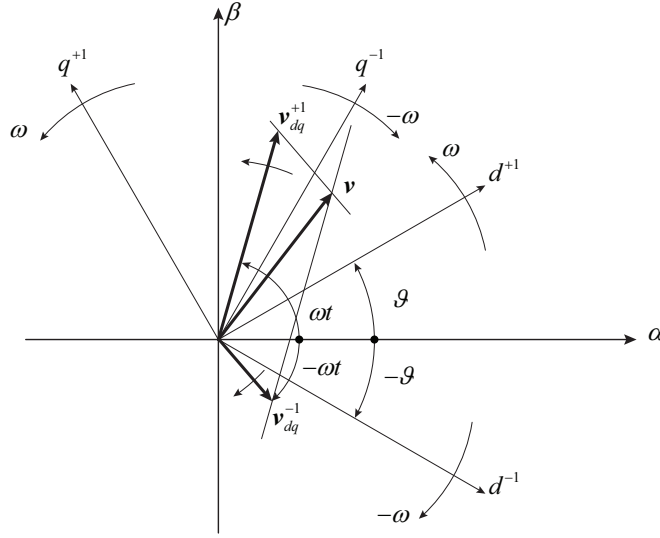
Figure 4.2: Voltage vector and axes of the DSRF.

If it is assumed that the angular position reference frame dq^{+1} matches the angular position of the positive-sequence voltage vector $\boldsymbol{v}^{+1}$, i.e. if $\vartheta = \omega t$, the unbalanced input voltage vector $\boldsymbol{v}$ can be expressed on the DSRF, yielding

$$\boldsymbol{v}_{dq}^{+1} = \begin{bmatrix} v_d^{+1} \\ v_q^{+1} \end{bmatrix} = \mathbf{T}_{dq}^{+1} \boldsymbol{v}_{\alpha\beta} = V^{+1} \begin{bmatrix} 1 \\ 0 \end{bmatrix} + V^{-1} \begin{bmatrix} \cos(-2\omega t) \\ \sin(-2\omega t) \end{bmatrix} \tag{4.3.1}$$

$$\boldsymbol{v}_{dq}^{-1} = \begin{bmatrix} v_d^{-1} \\ v_q^{-1} \end{bmatrix} = \mathbf{T}_{dq}^{-1} \boldsymbol{v}_{\alpha\beta} = V^{+1} \begin{bmatrix} \cos(2\omega t) \\ \sin(2\omega t) \end{bmatrix} + V^{-1} \begin{bmatrix} 1 \\ 0 \end{bmatrix} \tag{4.3.2}$$

where

$$\mathbf{T}_{dq}^{+1} = \left[\mathbf{T}_{dq}^{-1} \right]^T = \begin{bmatrix} \cos\vartheta & \sin\vartheta \\ -\sin\vartheta & \cos\vartheta \end{bmatrix} \tag{4.3.3}$$

Expression (4.3.1) and (4.3.2) are evidence that the DC values on the dq^{+1} and the dq^{-1} frames correspond to the amplitude of the sinusoidal signals of $\boldsymbol{v}^{+1}$ and $\boldsymbol{v}^{-1}$, while the oscillations at 2ω correspond to the coupling between axes appearing as a consequence of the voltage vectors rotating in opposite directions. Therefore, instead of using any filtering techniques for attenuating oscillation at 2ω, a decoupling network is presented in the following to completely cancel out the effect of such oscillations on the synchronous reference frame voltages of the PLL.

4.3.2 Decoupling network

To generalize the explanation of the decoupling network used in the DSRF, one suppose a voltage vector consisting of two components rotating with $n\omega$ and $m\omega$ frequencies respectively,

n and m can be either positive or negative. Therefore, this generic voltage vector is given by

$$\boldsymbol{v}_{\alpha\beta} = \begin{bmatrix} v_\alpha \\ v_\beta \end{bmatrix} = \boldsymbol{v}_{\alpha\beta}^n + \boldsymbol{v}_{\alpha\beta}^m = V^n \begin{bmatrix} \cos(n\omega t + \phi^n) \\ \sin(n\omega t + \phi^n) \end{bmatrix} + V^m \begin{bmatrix} \cos(m\omega t + \phi^m) \\ \sin(m\omega t + \phi^m) \end{bmatrix} \tag{4.3.4}$$

Additionally, two rotating reference frames are considered, dq^n and dq^m, whose angular positions are $n\vartheta$ and $m\vartheta$ respectively, where ϑ is the phase angle detected by the PLL. If a perfect synchronization of the PLL is possible, i.e. if $\vartheta = \omega t$, with ω the fundamental frequency, the voltage vector in (4.3.4) can be expressed on the dq^n and dq^m reference frames as follows

$$\boldsymbol{v}_{dq}^n = \begin{bmatrix} v_d^n \\ v_q^n \end{bmatrix} = \begin{bmatrix} \bar{v}_d^n \\ \bar{v}_q^n \end{bmatrix} + \begin{bmatrix} \tilde{v}_d^n \\ \tilde{v}_q^n \end{bmatrix} = \underbrace{V^n \begin{bmatrix} \cos \phi^n \\ \sin \phi^n \end{bmatrix}}_{\text{DC terms}}$$

$$\underbrace{+ V^m \cos \phi^m \begin{bmatrix} \cos\left((n-m)\omega t\right) \\ -\sin\left((n-m)\omega t\right) \end{bmatrix} + V^m \sin \phi^m \begin{bmatrix} \sin\left((n-m)\omega t\right) \\ \cos\left((n-m)\omega t\right) \end{bmatrix}}_{\text{AC terms}} \tag{4.3.5}$$

$$\boldsymbol{v}_{dq}^m = \begin{bmatrix} v_d^m \\ v_q^m \end{bmatrix} = \begin{bmatrix} \bar{v}_d^m \\ \bar{v}_q^m \end{bmatrix} + \begin{bmatrix} \tilde{v}_d^m \\ \tilde{v}_q^m \end{bmatrix} = \underbrace{V^m \begin{bmatrix} \cos \phi^m \\ \sin \phi^m \end{bmatrix}}_{\text{DC terms}}$$

$$\underbrace{+ V^n \cos \phi^n \begin{bmatrix} \cos\left((n-m)\omega t\right) \\ \sin\left((n-m)\omega t\right) \end{bmatrix} + V^n \sin \phi^n \begin{bmatrix} -\sin\left((n-m)\omega t\right) \\ \cos\left((n-m)\omega t\right) \end{bmatrix}}_{\text{AC terms}} \tag{4.3.6}$$

As shown by (4.3.5) and (4.3.6), the amplitude of the AC terms in the dq^n axes depends on the DC terms of the signals on the dq^m axes, and vice versa. Therefore, once the coupling terms between both reference frames are identified, a decoupling cell, can be designed to cancel out the oscillations generated by the voltage vector $\boldsymbol{v}^m$ on the dq^n axes signals. To cancel out the oscillations in the dq^m axes signals, the same structure may be used, but with swapping of the m and n indexes in it. In Figure 4.3, the DC terms on the dq^n axes are represented as $\bar{v}_d^m$ and $\bar{v}_q^m$.

As shown in Figure 4.4, a cross-feedback decoupling network is used to estimate the value of these DC terms on the positive and negative reference frames. In this decoupling network, the estimated DC terms are named as $(\bar{v}_d^m)^*$, $(\bar{v}_q^m)^*$, $(\bar{v}_d^n)^*$ and $(\bar{v}_q^n)^*$ and LPF block is a low pass filter such as

$$LPF(s) = \frac{\omega_f}{s + \omega_f} \tag{4.3.7}$$
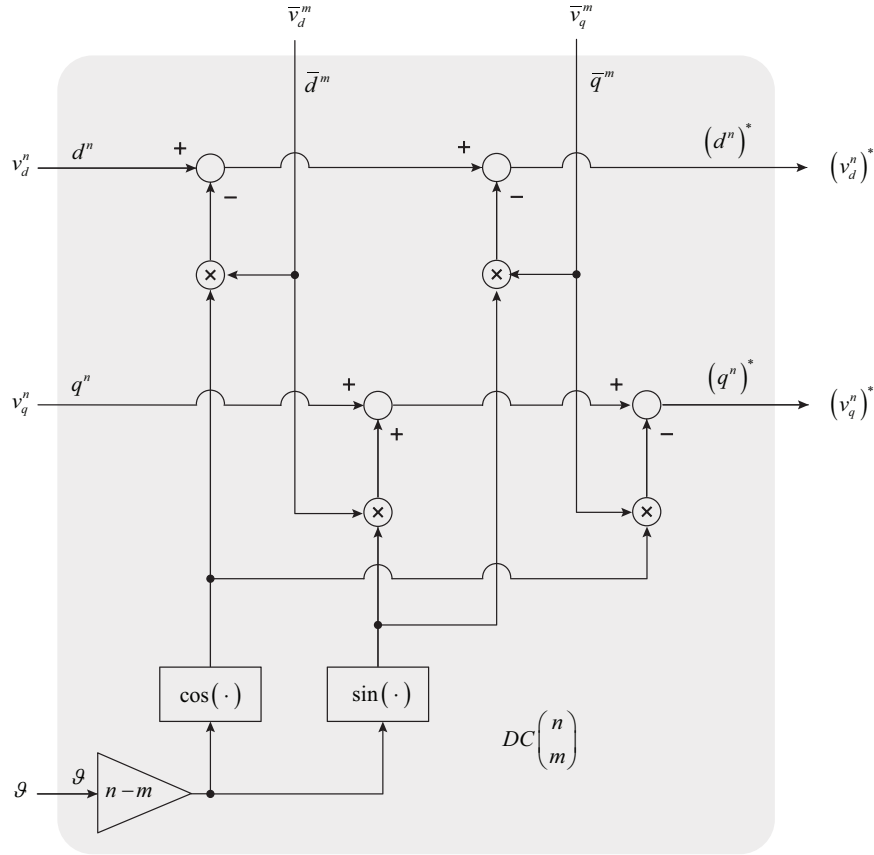
Figure 4.3: Decoupling cell for cancelling the effect of $\boldsymbol{v}^m$ on the dq^n frame signals.

The decoupled double synchronous reference frame (DDSRF) of Figure 4.4 allows free-oscillation signals to be obtained on the dq^m and dq^n reference frame. By setting $n = +1$ and $m = -1$, this network decouples information about the positive and negative sequence components of either voltage or current in unbalanced three-phase systems, which makes it a useful tool for synchronous controllers during unbalanced grid faults. This network can be used to decouple other frequency/sequence components simply setting the proper values for the m and n coefficients.

Figure 4.4: Decoupled double synchronous reference frame (DDSRF).

4.3.3   Analysis of the DDSRF

From Eq. (4.3.4), the unbalanced voltage during a grid fault, consisting of positive- and negative-sequence components at the fundamental frequency, can be generically expressed as

$$\boldsymbol{v}_{\alpha\beta} = \begin{bmatrix} v_\alpha \\ v_\beta \end{bmatrix} = \boldsymbol{v}_{\alpha\beta}^{+1} + \boldsymbol{v}_{\alpha\beta}^{-1} = V^{+1} \begin{bmatrix} \cos(\omega t + \phi^{+1}) \\ \sin(\omega t + \phi^{+1}) \end{bmatrix} + V^{-1} \begin{bmatrix} \cos(-\omega t + \phi^{-1}) \\ \sin(-\omega t + \phi^{-1}) \end{bmatrix} \tag{4.3.8}$$
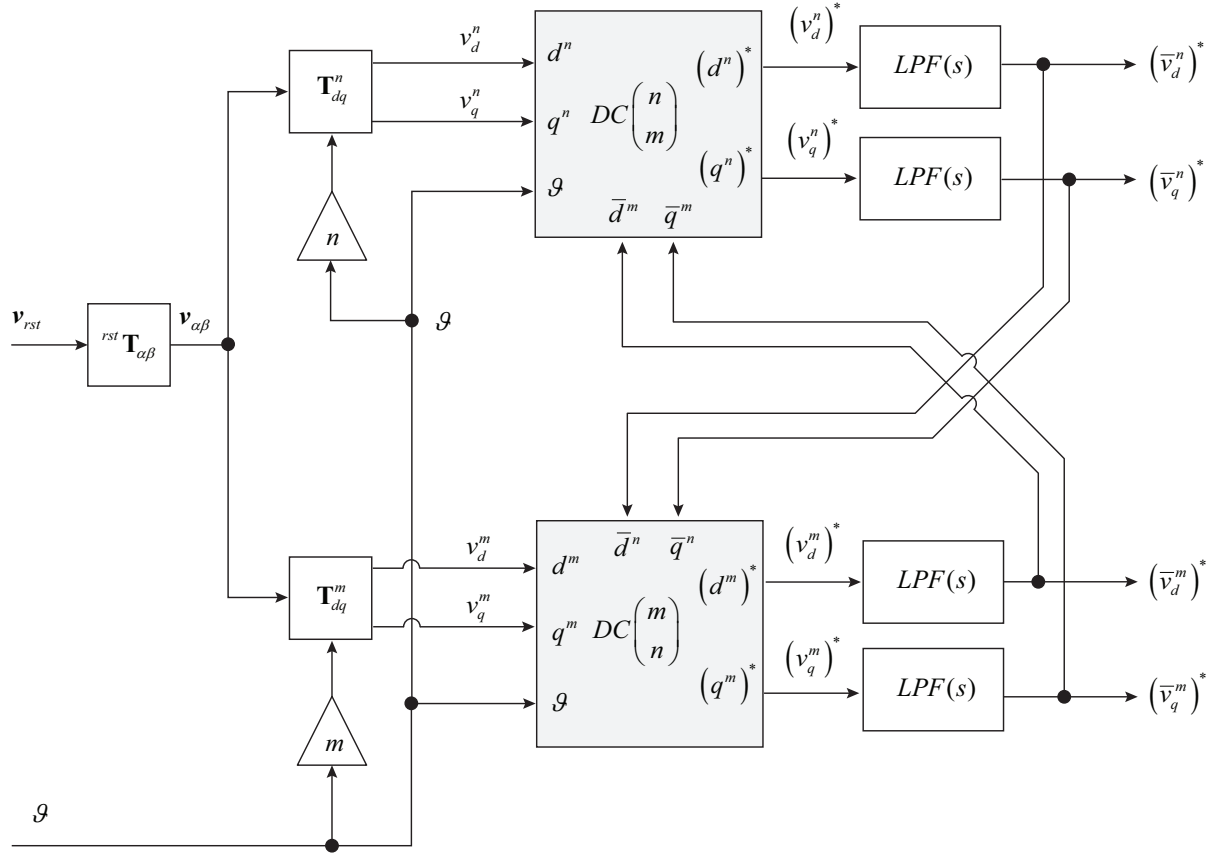
The projection of this voltage vector on the dq^{+1} and dq^{-1} reference frames can be easily obtained simply by setting $n = +1$ and $m = -1$ in (4.3.5) and (4.3.6). After rearranging equations, the dq signals on the positive and negative reference frames are given by

$$\boldsymbol{v}_{dq}^{+1} = V^{+1} \begin{bmatrix} \cos\phi^{+1} \\ \sin\phi^{+1} \end{bmatrix} + V^{-1} \begin{bmatrix} \cos\left(2\omega t\right) & \sin\left(2\omega t\right) \\ -\sin\left(2\omega t\right) & \cos\left(2\omega t\right) \end{bmatrix} \begin{bmatrix} \cos\phi^{-1} \\ \sin\phi^{-1} \end{bmatrix} \tag{4.3.9}$$

$$\boldsymbol{v}_{dq}^{-1} = V^{-1} \begin{bmatrix} \cos\phi^{-1} \\ \sin\phi^{-1} \end{bmatrix} + V^{+1} \begin{bmatrix} \cos\left(2\omega t\right) & -\sin\left(2\omega t\right) \\ \sin\left(2\omega t\right) & \cos\left(2\omega t\right) \end{bmatrix} \begin{bmatrix} \cos\phi^{+1} \\ \sin\phi^{+1} \end{bmatrix} \tag{4.3.10}$$

These expressions give evidence that the AC terms in the dq^{+1} axes result from the DC terms in the dq^{-1} axes being affected by a rotating transformation matrix at 2ω frequency. A similar conclusion can be obtained for AC signals of the dq^{-1} reference frame. These rotating transformation matrices are given b y

$$\mathbf{T}_{dq}^{+2} = \left(\mathbf{T}_{dq}^{-2}\right)^{T} = \begin{bmatrix} \cos(2\omega t) & \sin(2\omega t) \\ -\sin(2\omega t) & \cos(2\omega t) \end{bmatrix} \tag{4.3.11}$$

Therefore Eqs, (4.3.9) – (4.3.10) can be rewritten as follows

$$\boldsymbol{v}_{dq}^{+1} = \begin{bmatrix} v_d^{+1} \\ v_q^{+1} \end{bmatrix} = \bar{\boldsymbol{v}}_{dq}^{+1} + \mathbf{T}_{dq}^{+2}\bar{\boldsymbol{v}}_{dq}^{-1} \tag{4.3.12}$$

$$\boldsymbol{v}_{dq}^{-1} = \begin{bmatrix} v_d^{-1} \\ v_q^{-1} \end{bmatrix} = \bar{\boldsymbol{v}}_{dq}^{-1} + \mathbf{T}_{dq}^{-2}\bar{\boldsymbol{v}}_{dq}^{+1} \tag{4.3.13}$$

where

$$\bar{\boldsymbol{v}}_{dq}^{+1} = \begin{bmatrix} \bar{v}_d^{+1} \\ \bar{v}_q^{+1} \end{bmatrix} = V^{+1}\begin{bmatrix} \cos\phi^{+1} \\ \sin\phi^{+1} \end{bmatrix} \tag{4.3.14}$$

and

$$\bar{\boldsymbol{v}}_{dq}^{-1} = \begin{bmatrix} \bar{v}_d^{-1} \\ \bar{v}_q^{-1} \end{bmatrix} = V^{-1}\begin{bmatrix} \cos\phi^{-1} \\ \sin\phi^{-1} \end{bmatrix} \tag{4.3.15}$$

represent the amplitude of the sequence components applied to the input of the DDSRF. Thus, Eqs. (4.3.12) – (4.3.13) give evidence that the relationship between the signals on the positive and negative reference frames are given by

$$\boldsymbol{v}_{dq}^{+1} = \mathbf{T}_{dq}^{+2}\boldsymbol{v}_{dq}^{-1} \tag{4.3.16}$$

and

$$\boldsymbol{v}_{dq}^{-1} = \mathbf{T}_{dq}^{-2}\boldsymbol{v}_{dq}^{+1} \tag{4.3.17}$$

As a result, the estimated values of the output of the DDSRF can be written as follows

$$\left(\bar{\boldsymbol{v}}_{dq}^{+1}\right)^* = \begin{bmatrix} \left(\bar{v}_{d}^{+1}\right)^* \\ \left(\bar{v}_{q}^{+1}\right)^* \end{bmatrix} = \mathbf{F}(s)\left[\boldsymbol{v}_{dq}^{+1} - \mathbf{T}_{dq}^{+2}\left(\bar{\boldsymbol{v}}_{dq}^{-1}\right)^*\right] \tag{4.3.18}$$

$$\left(\bar{\boldsymbol{v}}_{dq}^{-1}\right)^* = \begin{bmatrix} \left(\bar{v}_{d}^{-1}\right)^* \\ \left(\bar{v}_{q}^{-1}\right)^* \end{bmatrix} = \mathbf{F}(s)\left[\boldsymbol{v}_{dq}^{-1} - \mathbf{T}_{dq}^{-2}\left(\bar{\boldsymbol{v}}_{dq}^{+1}\right)^*\right] \tag{4.3.19}$$

where

$$\mathbf{F}(s) = \begin{bmatrix} LPF(s) & 0 \\ 0 & LPF(s) \end{bmatrix} \tag{4.3.20}$$
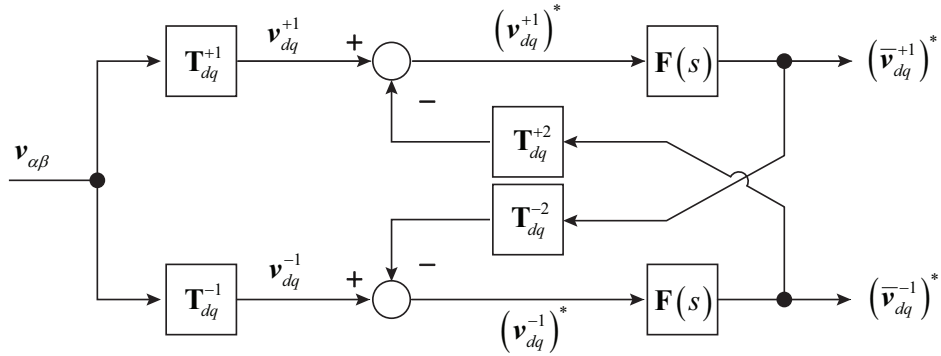

Figure 4.5: Block diagram of the DDSRF with $n = +1$ and $m = -1$.

Therefore, the DDSRF of Figure 4.4 can be represented for the particular case of the positive- and negative-sequence components at the fundamental frequency, as in Figure 4.5 shows. The estimation of the positive sequence component will be considered in the following. Substituting (4.3.19) into (4.3.18) it results

$$\left(\bar{\boldsymbol{v}}_{dq}^{+1}\right)^* = \mathbf{F}(s)\left[\boldsymbol{v}_{dq}^{+1} - \mathbf{T}_{dq}^{+2}\mathbf{F}(s)\left(\boldsymbol{v}_{dq}^{-1} - \mathbf{T}_{dq}^{-2}\left(\bar{\boldsymbol{v}}_{dq}^{+1}\right)^*\right)\right] \tag{4.3.21}$$

and using the relationship of (4.3.16) and (4.3.17), it results

$$\left(\bar{\boldsymbol{v}}_{dq}^{+1}\right)^* = \mathbf{F}(s)\left[\boldsymbol{v}_{dq}^{+1} - \mathbf{T}_{dq}^{+2}\mathbf{F}(s)\left(\mathbf{T}_{dq}^{-2}\boldsymbol{v}_{dq}^{+1} - \mathbf{T}_{dq}^{-2}\left(\bar{\boldsymbol{v}}_{dq}^{+1}\right)^*\right)\right] \tag{4.3.22}$$

rearranging, it results

$$\left(\bar{\boldsymbol{v}}_{dq}^{+1}\right)^* = \mathbf{F}(s)\left[\boldsymbol{v}_{dq}^{+1} - \mathbf{T}_{dq}^{+2}\mathbf{F}(s)\mathbf{T}_{dq}^{-2}\left(\boldsymbol{v}_{dq}^{+1} - \left(\bar{\boldsymbol{v}}_{dq}^{+1}\right)^*\right)\right] \tag{4.3.23}$$

The term $\mathbf{T}_{dq}^{+2}\mathbf{F}(s)\mathbf{T}_{dq}^{-2}$ will be now investigated

$$
\begin{aligned}
\mathbf{F}_{-2}(s) &= \mathbf{T}_{dq}^{+2}\mathbf{F}(s)\mathbf{T}_{dq}^{-2} \\[2mm]
&= \frac{1}{2}\begin{bmatrix} \big[\mathbf{F}(s+j2\omega)+\mathbf{F}(s-j2\omega)\big] & j\big[-\mathbf{F}(s+j2\omega)+\mathbf{F}(s-j2\omega)\big] \\ j\big[\mathbf{F}(s+j2\omega)+\mathbf{F}(s-j2\omega)\big] & \big[\mathbf{F}(s+j2\omega)+\mathbf{F}(s-j2\omega)\big] \end{bmatrix}
\end{aligned}
\tag{4.3.24}
$$

which results as follows

$$
\mathbf{F}_{-2}(s)=\mathbf{F}_{+2}^{T}(s)=\frac{1}{2}\begin{bmatrix} \frac{\omega_f(s+\omega_f)}{s^2+2s\omega_f+\omega_f^2+(2\omega)^2} & -\frac{\omega_f\omega}{s^2+2s\omega_f+\omega_f^2+(2\omega)^2} \\[3mm] \frac{\omega_f\omega}{s^2+2s\omega_f+\omega_f^2+(2\omega)^2} & \frac{\omega_f(s+\omega_f)}{s^2+2s\omega_f+\omega_f^2+(2\omega)^2} \end{bmatrix}
\tag{4.3.25}
$$

4.3.4   Structure of the DDSRF-PLL

The block diagram of the DDSRF-PLL is shown in Figure 4.6. As shown in the figure, this PLL is an extension of the conventional three-phase SRF-PLL structure. In this PLL, in order to obtain a similar dynamic response for different signal amplitudes, the phase-angle error signal v_q^{+1} is adaptively normalized to the amplitude of the positive-sequence input vector. Moreover, the rated grid frequency is added as a feed-forward parameter, ω_{ff}, to accelerate the tracking process of the PLL. The decoupling network of the DDSRF-PLL completely cancels out the oscillations at 2ω on the $d1^{+1}$ and $d1^{-1}$ reference frame signals.
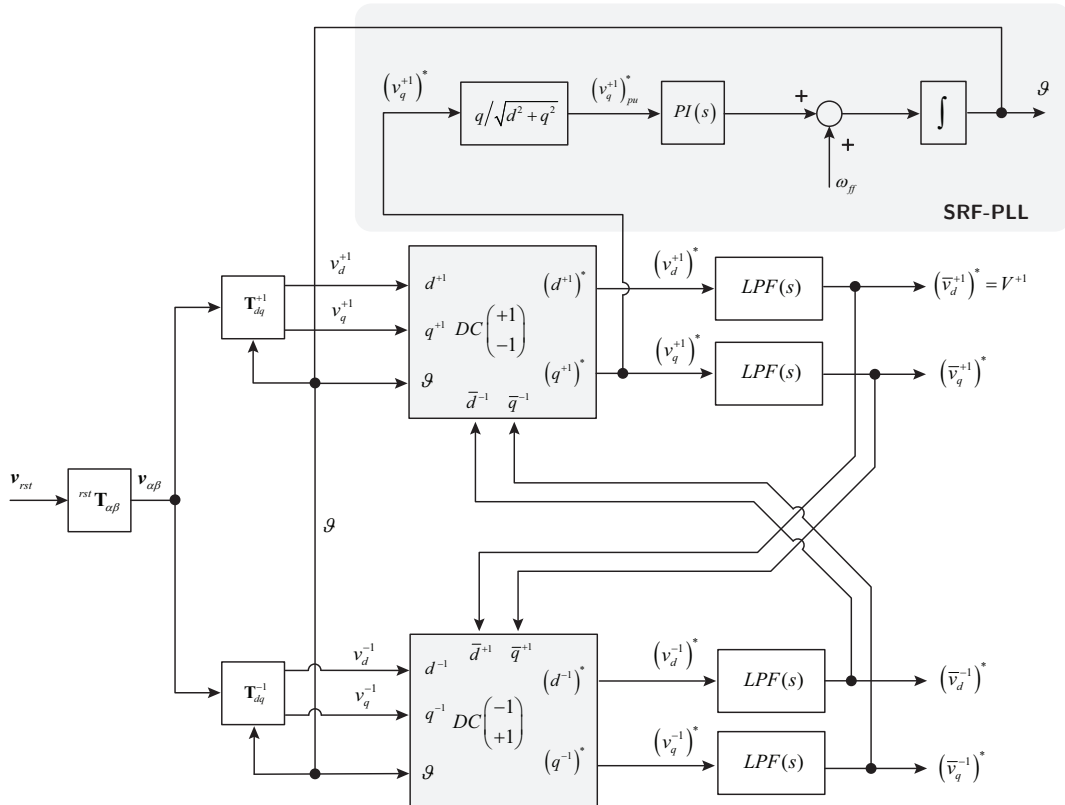

Figure 4.6: DDSRF PLL architecture.

$$\left[{}^{\alpha\beta}T_{dq}^{+1} \right] = \left[{}^{\alpha\beta}T_{dq}^{-1} \right]^{T} = \begin{bmatrix} \cos(\theta) & \sin(\theta) \\ -\sin(\theta) & \cos(\theta) \end{bmatrix}$$

$$\left[{}^{dq^{-1}}T_{dq}^{+2} \right] = \left[{}^{dq^{+1}}T_{dq}^{-2} \right]^{T} = \begin{bmatrix} \cos(2\theta) & \sin(2\theta) \\ -\sin(2\theta) & \cos(2\theta) \end{bmatrix}$$
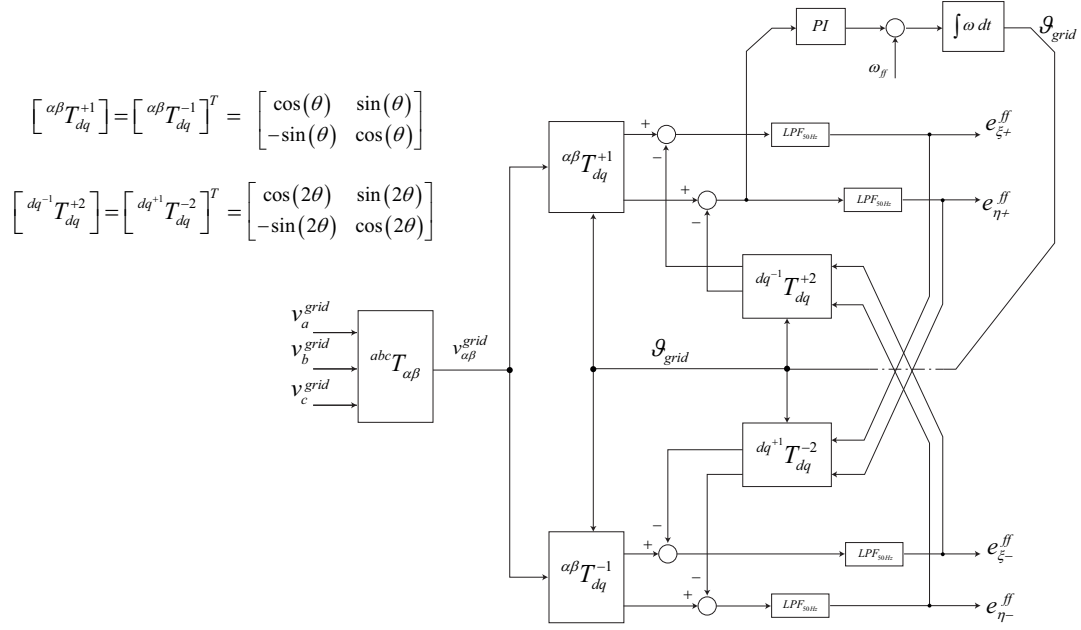

Figure 4.7: DDSRF PLL architecture - a different representation.

4.4   Simulation Results

In this section SRF-PLL and DDSRF-PLL performances are compared. Figure 4.8 shows a set of unbalanced grid voltages used as source for both pll architectures.
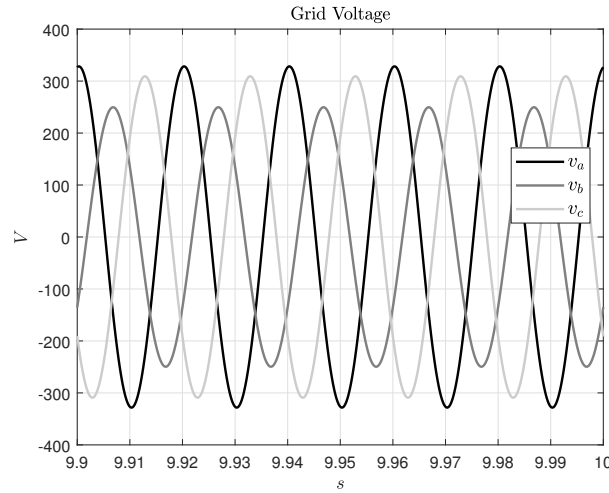

Figure 4.8: Grid voltage used for simulation analysis.

Figure 4.9a shows the performance for phase and frequency estimation of the SRF-PLL in case of unbalanced grid voltages. As can be seen, both of them are affected by a second component ($100\,\mathrm{Hz}$) harmonic generated by the fact the grid voltages are unbalanced.

(a) Phase and pulsation estimated by the SRF-PLL.

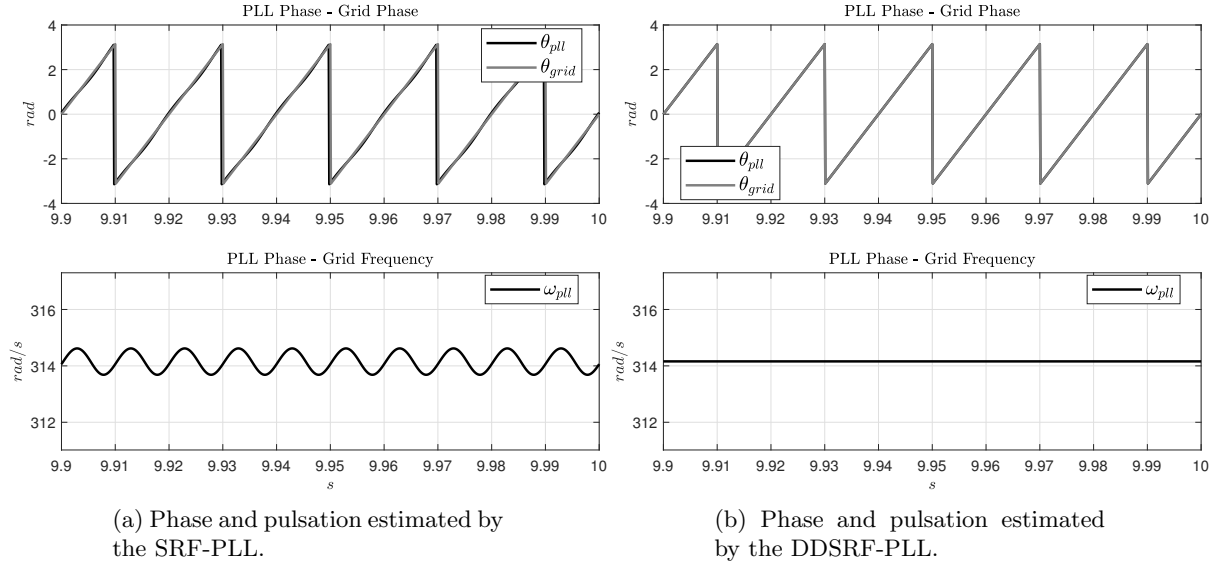(b) Phase and pulsation estimated by the DDSRF-PLL.

Figure 4.9: Simulation results.

Figure 4.9b shows the performance for phase and frequency estimation of the DDSRF-PLL in case of unbalanced grid voltages. As can be seen, the second harmonic which was present for the SRF-PLL case is completely compensated by the structure of the PLL, and estimated phase as well as estimated grid frequency results not affected by the unbalanced grid voltages.

Bibliography

[1] M. K. Kazimierczuk, D. Czarkowski, *Resonant Power Converters*. Wiley, 2nd Edition 2011.

[2] R. Teodorescu, M. Liserre, P. Rodrıguez, *Grid converters for photovoltaic and wind power systems*. Wiley, 2011.